2023

Fabrication and Characterisation of Large Area, Uniform and Controllable Surface Relief Patterns in Photopolymer Material

Owen Kearney
Technological University Dublin, Ireland, Owen.Kearney@tudublin.ie

Izabela Naydenova
Technological University Dublin, Ireland, izabela.naydenova@tudublin.ie

Funder: This research received no external funding

Fabrication and Characterisation of Large Area, Uniform and Controllable Surface Relief Patterns in Photopolymer Material

Owen Kearney[1,2], I. Naydenova[1,2*]

[1] School of Physics, Clinical and Optometric Sciences, Technological University Dublin, Dublin, Ireland

[2] Centre for Industrial and Engineering Optics, Technological University Dublin, Dublin, Ireland

Keywords. surface relief gratings, cross-grating, holography, photopolymers, optical patterning

ABSTRACT

As the risk of antibiotic resistant pathogens increases, development of convenient point of care devices is essential. Such devices would help avoid infection – ensure cleanliness of environments and assist in bacteria analysis.

The ultimate aim of the research presented here is to develop a compact, cost effective, easy to use optical device which is capable of detecting and quantifying bacteria in an aqueous sample. The surface relief patterns have a dual role, they provide a diffracted light signal, and control the adhesion of the bacteria to the surface. The strength of the diffracted signal is expected to provide a quantitative measure of the number of bacterial cells attached to the patterned surface.

An adjustable holographic set up for controlled patterning of a photopolymer surface using three-beams of varying intensity, incident angles, and state of polarisation was built. The system allows for the creation of surface relief cross-gratings (SRCG) of unit cell size ranging from 8 x 8 μm^2 (125 lines / mm) to as small as 1 x 1 μm^2 (1000 lines/ mm).

The surfaces are analysed via AFM, Phase contrast Microscopy, Fast Fourier transform analysis of the collected images and diffraction efficiency measurements. The surface relief amplitude dependence on recording parameters is investigated, the results demonstrate a strong dependence of the surface relief height on the period of the recorded structures. The largest surface relief amplitude achieved is 300 nm at 8 μm period. The possibility to achieve control over surface roughness by optical patterning was experimentally confirmed.

The production and characterisation of large area uniform SRCG, with controllable patterns will allow further experiments aiming at the development of bacterial assays to be completed, namely SRCG contact copying in water resistant materials and their functionalisation by coating.

1. INTRODUCTION

Qualitative and quantitative analysis of liquid environmental and clinical samples containing bacteria using microbiology methods, such as colony counting, is time-consuming, laborious and require particular skills as well as access to a microbiology lab [1]. Deadly infections caused by bacterial pathogens can be prevented if early and convenient point-of-care detection is available [2-4]. This is particularly important for priority I antibiotic-resistant pathogens (ARP), such as Escherichia coli, for which, according to the World Health Organisation (WHO), the development of new antibiotics is critical [6]. There are many countries throughout the world where standard antibiotic treatment of E-coli urinary tract infections, resulting from the presence of E-coli bacteria is deemed ineffective in more than half of patients [7]. The effect of surface roughness and its major role in the adhesion of bacteria to the surface has been clearly demonstrated in recent

years [8-9]. On the other hand, novel optical and photonic methods for detection of small number of bacteria, in contrast to the traditional microbiology methods where many bacteria are grown and examined, have been recently developed [1,5]. The main advantages of optical methods are immunity to external electromagnetic interferences, high sensitivity, parallel non-contact detection. To date, most light-based sensors use fluorescence, whereby target molecules, such as those on the bacterial cell wall, are labelled with fluorophores to indicate the presence, concentration, and activity of bacteria [10]. Fluorescent labelling complicates procedures, can interfere with bacterial viability, and requires prior knowledge of the bacteria to be labelled [11]. For that reason, there is an interest in label free techniques for detection of bacteria [1, 3].

The holographic approach to generating the surface structures yields a dual benefit for the detection of microorganisms. First, control of the surface morphology and thus facilitating cell's adhesion, and second, a measurable diffraction output, representative of the surface morphology.

Holographic recording was previously used to create periodical structures, of controllable period in photopolymer material [12-16].

The size and height of the surface structures was demonstrated to be dependent on the composition of photopolymer used. This allows the surface roughness to be varied, as the surface structure period is varied. It is expected to see a clear relationship between roughness and bacterial attachment, as the SRCGs are homogenously patterned/roughened. Due to the complex nature of the interaction between bacteria and the surface, different dependence of the bacteria adhesion on the surface roughness has been reported in the literature. Some studies report that reduction in surface roughness leads to decreased bacteria adhesion [7,17,18], in other cases the reduction in surface roughness has been observed to lead to increased bacteria adhesion [9,19], while in [20,21] both regimes were observed, concluding that behaviour differed between different bacteria, and that mean roughness was insufficient to establish a direct correlation. Lack of dependence of bacteria adhesion on the surface roughness has been reported in [22]. The previous studies reveal that the surface roughness is not the only parameter playing an important role. They emphasise the need for further studies and the importance of being able to control the surface physical and chemical properties.

2. BACKGROUND

This section describes the geometrical considerations taken into account when building the holographic recording set-up. It concerns the relative positions of the three recording beams as well as their state of polarisation in view of achieving the flexibility to inscribe all 2D- Bravais lattices. It follows an approach first introduced by Escuti at all [23].

2.1 RECORDING BEAMS POLARISATION STATE AND INTENSITY REQUIREMENTS

The proposed holographic recording set-up utilises three coherent laser beams. To achieve the desired interference pattern to be copied in the photosensitive material a careful adjustment of the state of polarisation and the intensities of the three recording beams is required. In the general case each pair of beams will produce three sets of interference fringes. Each set of fringes has a spatial period depending on the angle between the corresponding pair of beams.

To achieve only two overlapping interference patterns from a set of three coherent beams, one of the resulting three interference patterns needs to be eliminated. This can be achieved if two of the recording beams are mutually orthogonal ($\theta = 90°$) Equation 1, in this case their interference pattern has zero fringe visibility V.

$$V = \mu \frac{2E_1E_2}{E_1^2+E_2^2} \cos(\theta) \quad (1)$$

Where V is the fringe visibility, μ is the spatial coherence, and E_1, E_2 are the electric fields of the interfering waves, θ is the angle between the planes of polarization of the two waves.

Figure 1 shows the state of polarisation of the three beams and the corresponding interference patterns created by each pair of beams, as well as the final pattern generated by a MATLAB programme, beam 1 and beam 3 have orthogonal

polarisations, hence they do not produce an intensity varying pattern. As seen from equation 1, to achieve maximum fringe visibility the polarisation of the two interfering beams must be parallel, and their intensities must be equal.

In the proposed optical set-up, beam 2 is linearly polarised at 45°with respect to the other two beams. Its horizontal component interferes with beam 3 and its vertical component interferes with beam 1. To improve the visibility of the generated interference patterns, the 45° polarised beam must have twice the intensity of the other two beams. The relative intensities of the three beams as they propagate through the optical system are shown in figure 2A, satisfying the condition for maximum fringe visibility, given the polarisation state requirements.

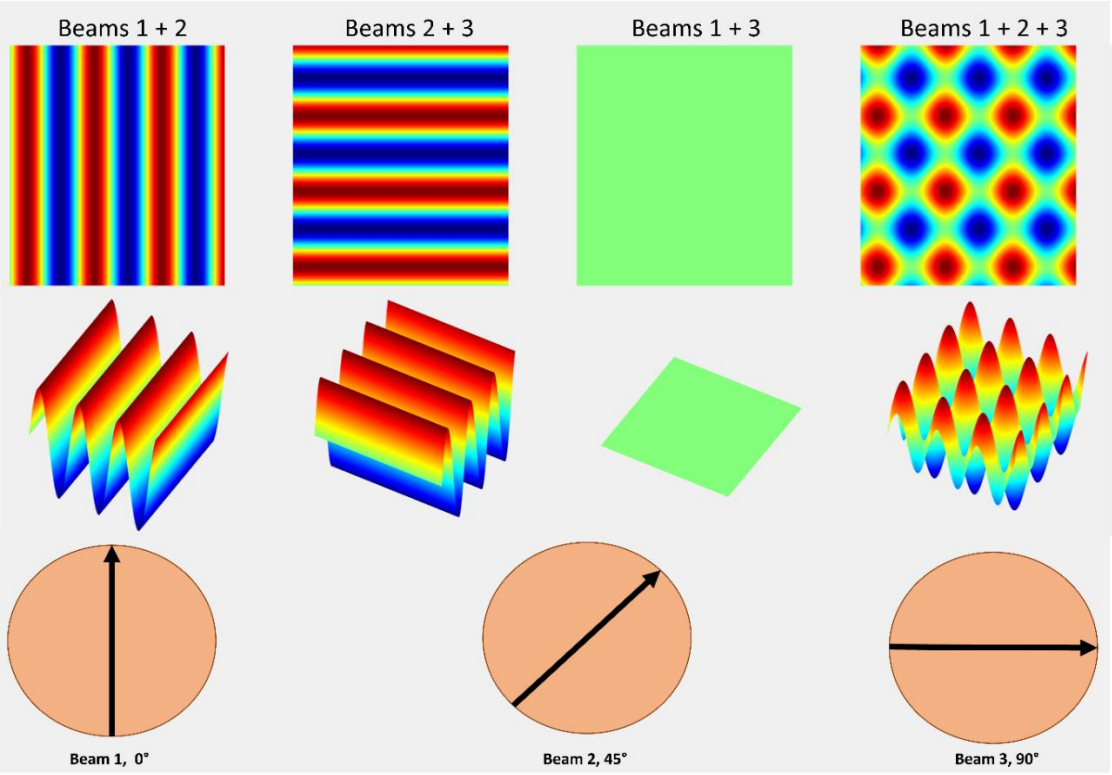

Figure 1. Diagram showing the interference pattern created from the superposition of each beam pair. 2d and 3d images are given for clarity. Beneath is a diagram showing the polarisation state of each beam required to obtain the above interference patterns.

2.2 CONTROL OVER THE OPTICAL PATTERN

The apparatus was designed to cover a range of spatial periods and the possibility to create all types of 2D-Bravais lattices. To achieve a desired spatial frequency, the angle each beam makes to the interference plane must be controlled by altering the geometry of the system (figure 2). The following equations were used in calculating the spatial parameters of the system:

$$a = \frac{\lambda}{|\sin\theta(\cos\phi 1 - \cos\phi 2)|} \tag{2}$$

$$b = \frac{\lambda}{2|\sin\theta \sin\phi 2 \sin\left(\frac{\phi 1+\phi 2}{2}\right)|} \tag{3}$$

$$\gamma = \frac{\phi 1+ \phi 2}{2} \tag{4}$$

Where $\phi_{1,2}$ – azimuthal angles, θ – propagation angle of the beams, (figure 2), λ = wavelength of light,

a and b are the real-space lattice constants and γ is the angle between the primitive vectors a and b of the cell to be inscribed on the surface [23]. Furthermore, also derived in [23], the azimuthal angles (illustrated in figure 2 B) of the beams can be calculated with the help of equations 5 – 8.

$$\phi 2 = \tan^{-1}\left(\frac{\sin\gamma}{\cos\gamma - (b/a)}\right) \quad (5)$$

$$\phi 1 = 2\gamma - \phi 2 \quad (6)$$

$$\phi 3 = -\phi 2 \quad (7)$$

$$\theta = \sin^{-1}\frac{\left(\frac{\lambda}{b}\right)}{2\sin\phi 2\,\sin\gamma} \quad (8)$$

Equations 2 – 8 can be used to calculate the required propagation angles of the beams for a given set of real space lattice constants. Hence the required positioning of optical components for all 5 2D Bravais lattices can be calculated.

A new angle is introduced in [24], α defined as ϕ2 – ϕ1. α is the angle made, between beam 2, and the horizontal plane on which beam one and three lie. Angle θ influences the period of the interference patterns, while α influences the unit cell shape. The geometry of the three beams and the sample holder arrangement is illustrated in figure 2 below.

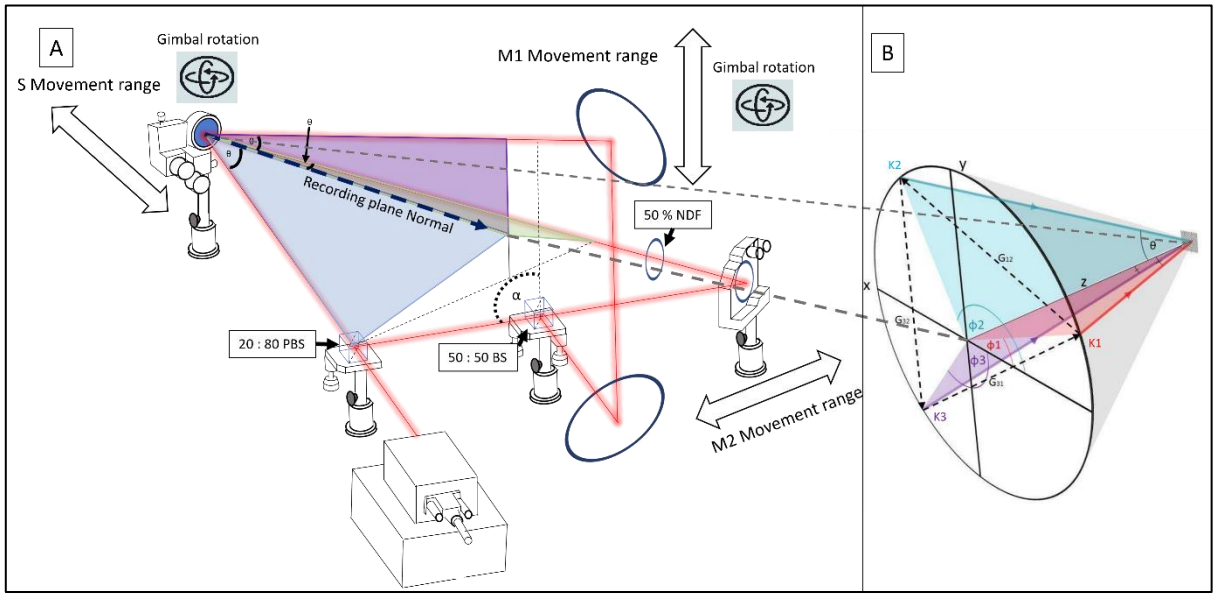

Figure 2. A) 2D illustration of the three beam recording apparatus, illustrating the required relative beam angles to the recording plane, θ. α, the angle made, between beam 2, and the horizontal plane, the movement range of mirror 1, mirror 2 and the sample holder, highlighted also is the recording plane normal. The intensity modulation of the apparatus is also described as the beam propogates through the system. B) Beam profile, illustrating azimuthal angles relative to beam position.

Mirrors M_1 and M_2 and sample holder S, as labelled in figure 2 can be moved along a single axis. M_1 and S are set in Gimbal mounts to allow their rotation in two axis, to achieve the correct positioning of the beams, and recording plane.

3. MATERIAL AND METHODS

3.1 THREE BEAM RECORDING APPARATUS DESIGN

Figure 3 shows a 3D render of the apparatus used to record the SRCGs into photopolymer. The following will explain the details of the apparatus design.

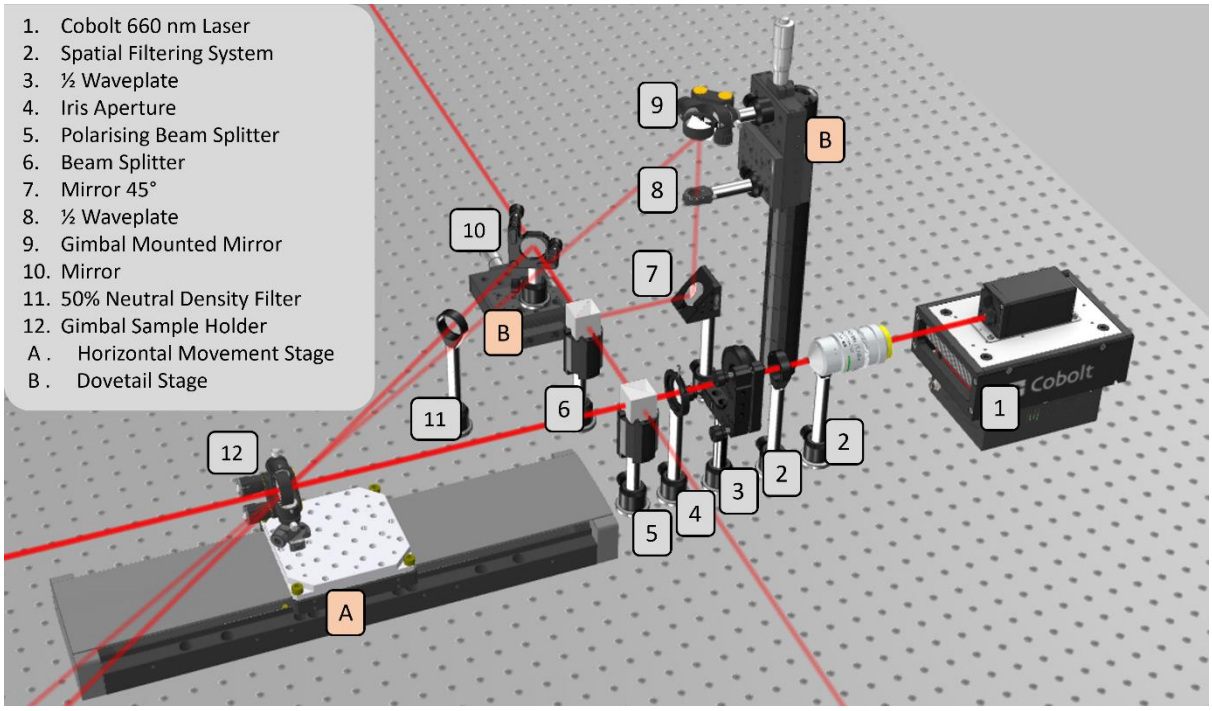

Figure 3 Three-beam holographic recording set-up for optical patterning of photosensitive materials. The optical components are labelled and named in the legend.

A 660 nm beam from a Cobolt-Flamenco laser (1) is first spatially filtered, expanded, and collimated (2), before approaching the first halfwave plate (3). This halfwave plate is used to adjust the beam polarisation prior to entering the polarising beam splitter. An aperture (4) is used to determine the beam size. The polarising beam splitter (5) (PBS) splits the beam into two beams propagating in orthogonal directions. Each beam has orthogonal polarisation, the intensity of each is dependent on the initial polarisation state of the beam entering the PBS. Beam 1 is directly incident on the recording plane (12). Beam 2 is directed towards a second non polarising 50:50 beam splitter (6) (BS). One of the beams emerging from BS (beam 3) is reflected from a mirror (10) and passes through a 50% neutral density filter (11), this is to control the beam intensity needed for achieving maximum contrast of the fringes. After the BS, beam 2 is reflected from a mirror (7) and passes through a 1/2 WP (8) to adjust the beam polarisation, it then is reflected from mirror (9) and is sent towards the interference plane. At the interference plane is a gimbal mount rigged to mount a glass slide coated in a photopolymer. The slide is oriented with its normal parallel to the recording plane normal, as illustrated in figure 2. A, B represent linear movement stages, these stages allow repositioning of the mirrors, and the sample holder. Both the sample holder and mirror (9) are mounted in 360° Gimbal mounts, allowing the required orientation of these components. To change the spatial frequency of the recording interference, pattern the position of mirror (9) (10) and gimbal sample holder (12) must be adjusted.

3.2 PREPARATION OF PHOTOPOLYMER SOLUTION

The diffraction gratings are recorded in an acrylamide-based photopolymer, using Methylene Blue (MB) as the dye sensitiser and triethanolamine as the initiator. The chemical composition, previously optimised to the recording of surface relief gratings [12], is shown in table 1.

The 10 % w/v PVA mixture was prepared by mixing PVA powder in water, heated at 85°C. The solution was stirred by a magnetic stirrer until fully dissolved. The MB stock solution 1.1 mM was prepared by adding 0.11g of MB to 100 ml deionised water. To fully dissolve the MB, the solution was left in a sonic bath for 5 minutes.

Table 1. Table listing the chemical composition of photopolymer.

Substance	Quantity	Unit
10% Polyvinyl alcohol (PVA)	17.5	ml
Triethanolamine (TEA)	1	ml
Acrylamide (AA)	1	g
N,N Methylene Bis-Acrylamide (BA)	0.2	g
Methylene Blue 1.1mM (MB)	4	ml

3.3 PREPARATION OF PHOTOPOLYMER LAYERS

Each layer was prepared in a dark room to avoid unwanted reaction of the photopolymer with light. The photopolymer was measured out onto a clean glass slide using a micropipette. Photopolymer solution with volume of 300 μl was spread uniformly on the glass slide thus yielding a sample thickness of ~30 μm after drying. The samples were left to set for 6 hours, before being recorded.

3.4 RECORDING PROCESS

To record a cross-grating with the desired spatial period mirrors (9), (10) and the sample holder (12) must be positioned correctly, as discussed earlier.

The photopolymer samples were allowed 15 minutes to adjust to the recording rooms temperature and humidity. After which each sample was positioned within the sample holder. A diffraction pattern was recorded. Each pattern was recorded at an intensity of 1.134 mW/cm^2 for 60 seconds with the 660 nm Cobolt-Flamenco laser. The recording intensity and time was chosen after a preliminary investigation into the quality of recorded gratings, at a range of intensity and times.

3.5 POST-RECORDING SAMPLE TREATMENT

After the initial recording procedure was completed, each sample was exposed to UV light **(**Mega Electronics, model 5503-11, 2.5 mW/cm^2) for 30 minutes. This was carried out to fully polymerise the photopolymer layer, to prevent further uncontrolled light polymerisation, and to prevent relaxation of the formed pattern due to diffusion of the unpolymerized monomer.

After UV treatment the samples underwent thermal exposure to enhance surface relief amplitude. The thermal treatment was carried out in a fume hood. The oven (Memmert model UNB 100) was initially set at 70 °C and the temperature was gradually increased in increments of 10 °C every 10 minutes, until the temperature had reached 220 °C, after which the samples were left for a further 10 minutes at 220 °C, before being removed from the oven.

3.6 CHARACTERISATION OF THE SAMPLES BY PHASE CONTRAST AND ATOMIC FORCE MICROSCOPY

Phase contrast microscope images (PCM) images were taken using an Olympus BX51 Phase contrast microscope with an Olympus Uplan FL N objective, at 40 x magnification, imaged with an Olympus DP72 Camera using Cell^{B} software. AFM images were taken using a Nanosurf Easyscan 2 atomic force microscope, with a 70 µm scan head in static force mode with a PPP-Contr 20 cantilever tip 0.02 – 0.77 N/m force constant.
The diffraction efficiency of the recorded SRCG was estimated by measuring the intensity of a probe beam before, I_0 and after, I_1, passing through the SRCG, with the help of equation 9.

$$\eta = (I_0 - I_1)/I_0 \quad (9)$$

4. RESULTS AND DISCUSSION

4.1 ESTABLISHING CONTROL ON FEATURE PERIOD

In order to demonstrate that the system could be used to generate surfaces of varying spatial period the apparatus was set to record a 2 µm, 5 µm and 8 µm spatial period SRCG. After recording the samples underwent post recording UV and thermal treatment. The SRCGs were scanned using PCM and AFM. The spatial period of each grating was determined, for each direction of symmetry within the SRCG. Figure 4 A shows the three directions measured on an 8 µm spatial period SRCG, and Table 2 compares the expected spatial frequency to the actual spatial frequency measured. The difference between layers recorded with different spatial period, measurable by both AFM and PCM is illustrated in figure 4 B.

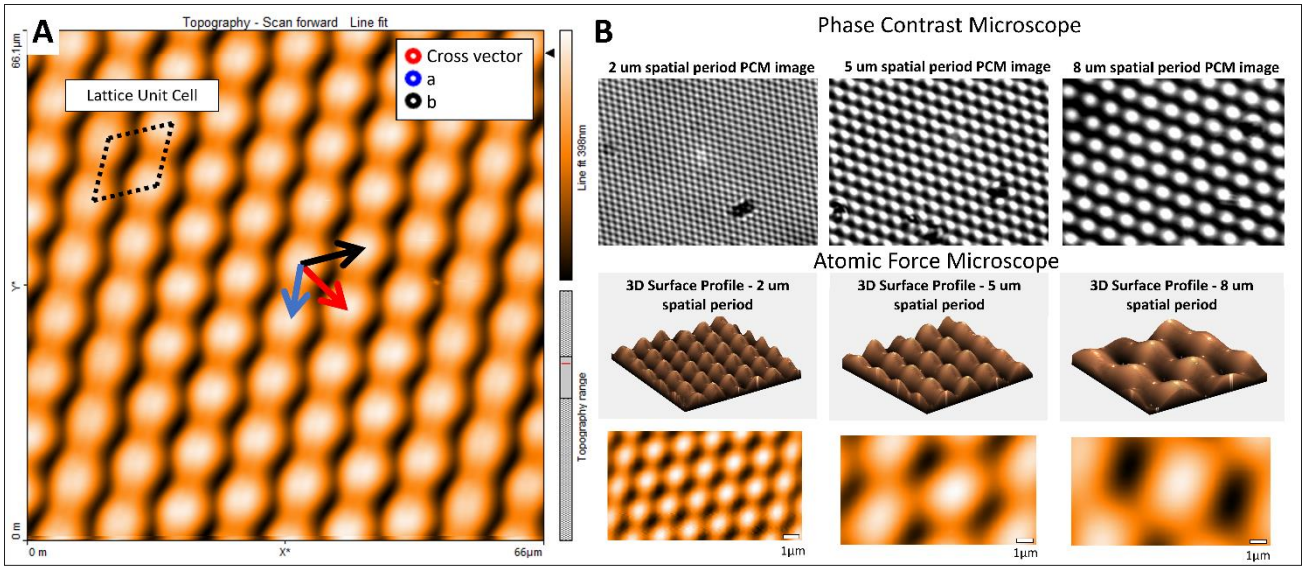

Figure 4. A) AFM image of an 8 µm SRCG with labelled direction vectors, and a labelled Lattice unit cell. B) PCM images, AFM images in 2-D and 3-D Illustrating control of the surface feature period.

Table 2. Table showing the expected period of surface features, and the measured period in the a, b, and cross vector directions, as illustrated in figure 4. The angle between the 2nd and a and b vectors are also given in the table, along with the maximum deviation in period to that expected.

Expected Period (μm)	Cross vector length (μm)	a (μm)	b (μm)	γ (°)	Maximum deviation from expected period %
2	2.284	2.392	2.488	124.222	24.4
5	5.175	5.200	5.266	120.736	5.3
8	7.800	7.950	8.300	122.678	3.8

Table 2 shows that the spatial frequency in each direction for a single grating differs within 3.8% (8μm), 5.3 % (5μm) and 24% (2μm) from the expected period. There is a trend showing that the spatial period in each direction increases as the direction measured changes from cross vector to a to b. The cross-vector angle is expected to remain constant as the feature period is changed, as the SRCG's are being changed in size only and not shape. There is a variance of ~ ± 2 ° observed.

4.2 DIFFRACTION PATTERN ANALYSIS

The diffraction patterns produced by the SRCGs is unlike that of a standard line grating. There is three-fold symmetry of the surface features which leads to the light experiencing diffraction analogous of three separate line gratings superimposed. While it was expected to see diffraction of just two superimposed gratings, the third line grating is attributed to slight misalignment of the three-beam system, allowing intensity variation due to interference between the first and third beam pair. Figure 5 shows the expected diffraction of the SRCG, when only two beam-pairs are interfering A), the expected diffraction when the third beam pair contributes to the interference pattern B), the estimated diffraction pattern of a real SRCG calculated via Fast Fourier Transform of the AFM image of the surface C) and compared with the diffraction of the SRCG illuminated via a 660 nm wavelength laser D). The SRCG diffraction imaged in figure 5 D) shows multiple orders, appearing to have relatively high intensity, due to the camera sensitivity. As can be seen in table 4, the diffraction efficiency percentage, the fraction of intensity not in the zeroth order is quoted as between 20 ~ 40 %, depending on grating period. Figure 5 A - B) are calculated by simulating the grating, and then taking the Fourier transform of the simulated grating. Similarly Figure 5 C) was calculated, using AFM surface topography data.

The contribution to the final SRCG by each interfering beam pair was investigated, by recording patterns in photopolymer with each beam pair alone. The relative surface height in each SRCG was compared and is shown in table 3. It was estimated that there is a contribution of about 14 % from the third beam pair. In addition, the ability of the photopolymer to copy the interference pattern has some limitations. This could also contribute to the difference in expected vs measured diffraction pattern.

Table 3. Table of percentage contribution of each beam pair to the final pattern, in the three-beam apparatus.

beam pair	Contribution to full pattern (%)
1 + 2	37.79
2 + 3	47.87
1 + 3	14.34

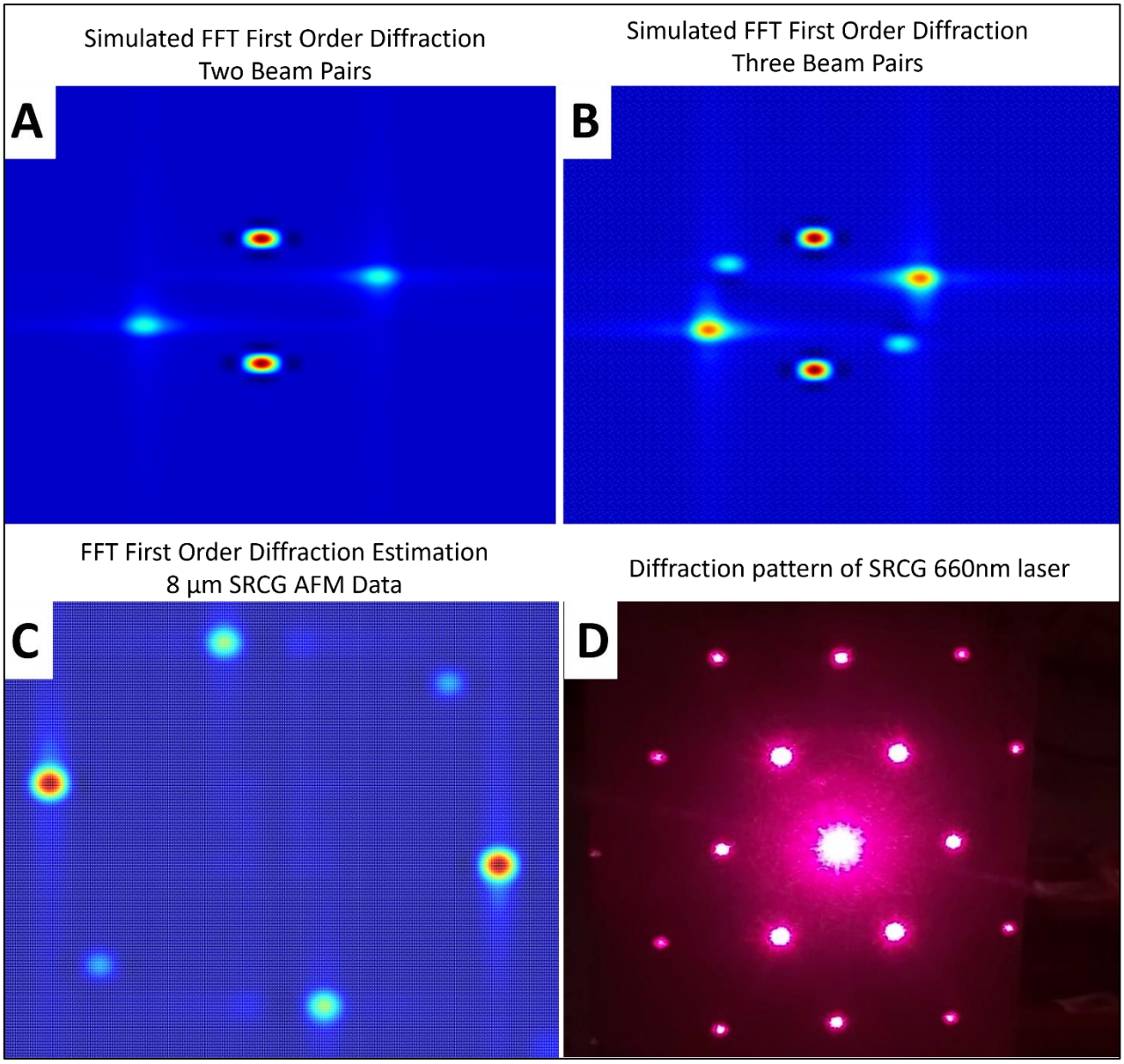

Figure 5. Figure illustrating A) Fast Fourier transform, estimated diffraction pattern, interference of two beam pairs. B) Fast Fourier transform estimated diffraction pattern, interference of three beam pairs. C) Fast Fourier transform, diffraction pattern, of an 8 µm SRCG, and D) Diffraction pattern of an SRCG illuminated with a 660 nm wavelength laser.

The diffraction efficiency of the recorded SRCGs was calculated by measuring the intensity before and after the SRCG, following the procedure described in 3.6, and is shown in table 4. The diffraction efficiency increased, as the feature period was increased. This is expected as at lower spatial frequency the surface relief amplitude was measured to be larger. Fourier analysis of the AFM images of the surfaces, allows the diffraction pattern to be predicted, in both relative position and intensity distribution as imaged in figure 5 C). Fourier transforms of the surface topography of a 2,5 and 8 µm SRCGs measured by AFM, was calculated. A plot of the relative diffraction pattern positioning of the SRCGs, at a constant distance from the diffraction plane was created, shown in figure 6.

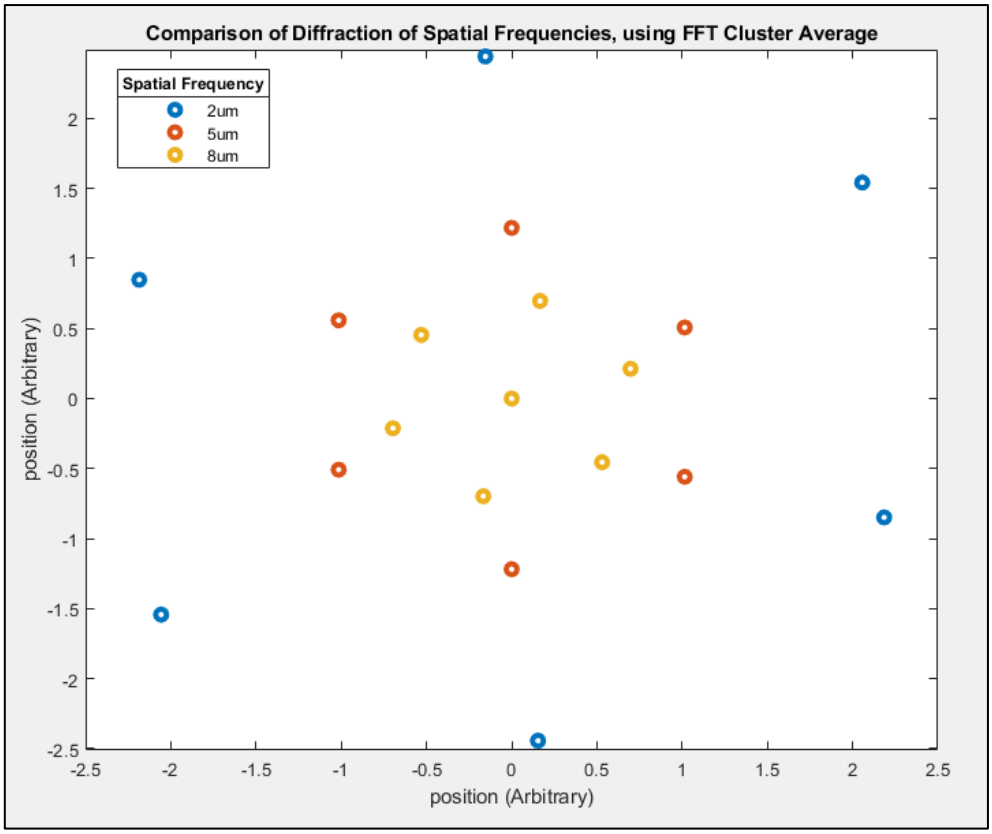

Figure 6. Graph showing the relative position of the estimated diffraction patterns, of the 2,5 and 8 µm SRCG's, as imaged at a constant distance from the diffraction plane. The patterns are centred at zero to help illustrate their differences.

Figure 6 shows a good agreement between the predicted diffraction pattern, calculated by Fourier analysis of AFM images of the surface, vs captured actual position of the diffraction orders figure 5D).

4.3 SURFACE ROUGHNESS ANALYSIS

The area roughness of each surface was calculated for each AFM scan of the SRCGs. Both the average roughness and RMS roughness are quoted for each SRCG in table 4**.** The roughness of the SRCGs exhibits a positive correlation with increasing feature period. Due to the homogeneity of the SRCGs, the majority of the changes in roughness is attributed to the change in grating height, as the feature period is varied. Being able to control the surface roughness will allow for future systematic studies of the dependence of cell adhesion versus properties of the patterned surface.

Table 4. Table comparing the expected Period of the SRCG's, with the surface roughness, rms, and average, in nm. Compared with the diffraction efficiency of the SRCG's.

Expected Period (µm)	AreaRoughness rms (nm)	Area Roughness avg (nm)	DE% 0th order
2	15.779	13.081	22.20
5	21.562	17.844	26.41
8	95.348	80.706	42.57

4.4 DEPENDENCE OF GRATING HEIGHT ON FEATURE PERIOD

There is a dependence of the SRCG feature height on the SRCG feature period as previously noted for a single grating studied in [12]. This dependence was investigated in the three-beam configuration. The apparatus was set to record at the appropriate feature period. Six SRCGs were recorded at (1.134 mW/cm^2 for 60 seconds), for three spatial periods, 2um, 5um and 8um. Using data measured with the AFM, the feature height, and the actual spatial period of each SRCG was investigated. The SRCG feature height and Period was averaged and plotted in figure 7. Figure 7 shows a positive correlation between the SRCG feature period and the height, The surface height vs feature period was plotted for each direction of symmetry on the SRCG, from figure 7**,** the cross vector direction exhibited both greater spatial period, and feature height, than that of direction a or b.

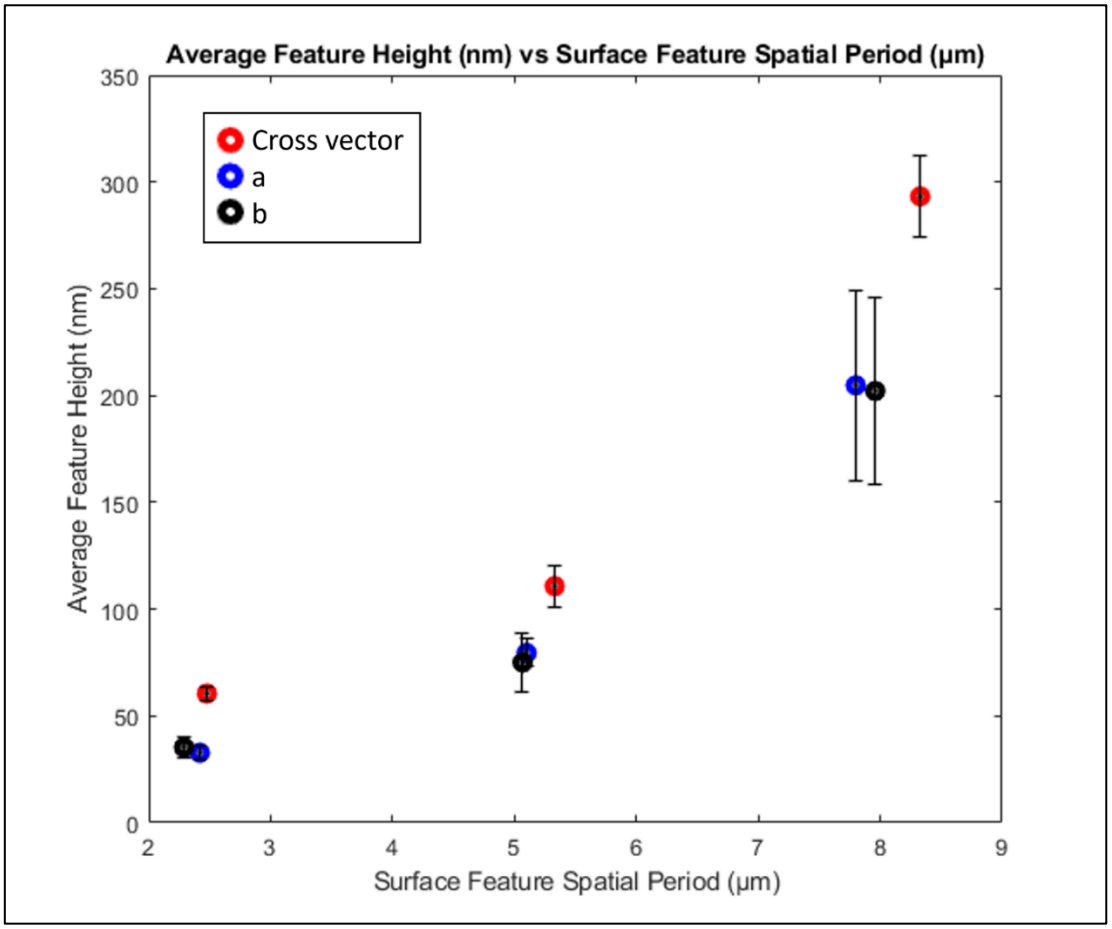

Figure 7. Graph of the average SRCG feature height in nm, vs the SRCG feature period in µm.

5. CONCLUSION

A three-beam optical system for single exposure recording of crossed gratings was designed, built, and demonstrated. Gratings of 2, 5 and 8 um feature period were produced and characterised, demonstrating a range of spatial periods the system is capable of recording. The photopolymer used exhibited a relationship of recording period and feature height where the greater feature period exhibited greater feature height, this directly effected the roughness of each layer. The

initial studies demonstrate that it is possible to change the surface roughness by a factor of six (from 15 to 95 nm) by changing the period of the inscribed surface relief features (from 2 to 8 μm).

6. FURTHER WORK

The ability to produce surfaces with controlled roughness and periodicity will allow further testing in the ability of the surfaces to adhere bacteria, namely Escherichia coli. The surface conditions can be modified, and the adherence % compared. Preliminary studies demonstrate that the surfaces can be successfully copied in a water-resistant material, such as PDMS, other materials are also being considered. The optimised conditions for obtaining high fidelity copies will be published elsewhere.

7. REFERENCES

[1] Giampaolo Pitruzzello*, Donato Conteduca and Thomas F. Krauss, Nanophotonics for bacterial detection and antimicrobial susceptibility testing, Nanophotonics 2020; ▪▪▪(▪▪▪): 20200388, published online on 15 September 2020; https://doi.org/10.1515/nanoph-2020-0388.

[2] George Luka, Ali Ahmadi, Homayoun Najjaran, , Evangelyn Alocilja, Maria DeRosa, Kirsten Wolthers, Ahmed Malki, Hassan Aziz, Asmaa Althani and Mina Hoorfar, Microfluidics Integrated Biosensors: A Leading Technology towards Lab-on-a-Chip and Sensing Applications, Sensors 2015, 15, 30011–30031; https://doi:10.3390/s151229783.

[3] Nuno Miguel Matos Pires, Tao Dong, Ulrik Hanke and Nils Hoivik, Recent Developments in Optical Detection Technologies in Lab-on-a-Chip Devices for Biosensing Applications, Sensors 2014, 14, 15458-15479; https://doi:10.3390/s140815458.

[4] Wang, P., Sun, H., Yang, W., Fang, Y., 2022. Optical Methods for Label-Free Detection of Bacteria. Biosensors 12, 1171. https://doi.org/10.3390/bios12121171

[5] Bo Ram Choi, Juyeon Cho, Jooyeong Kim, Ji SuKim, Kyungjin Kim, and Hyukjin Lee, Capillary Tube Based Molecular Diagnostic Test for Naked Eye Detection of Antibiotic Resistant Bacteria, Adv. Mater. Technol. 2019, 4, 1800375; DOI: 10.1002/admt.201800375.

[6] WHO, http://www.who.int/drugresistance/documents/situationanalysis/en (accessed: October 2020)

[7] WHO, https://www.who.int/news-room/fact-sheets/detail/antimicrobial-resistance(accessed:November 2022)

[8] Lucas Costa de Medeiros Dantas, João Paulo da Silva-Neto, Talita Souza Dantas, Lucas Zago Naves, Flávio Domingues das Neves, and Adérito Soares daMota, Bacterial Adhesion and Surface Roughness for Different Clinical Techniques for Acrylic Polymethyl Methacrylate, International Journal of Dentistry Volume 2016, Article ID 8685796, 6 pages, http://dx.doi.org/10.1155/2016/8685796.

[9] Songmei Wu, Stefanie Altenried, Andi Zogg, Flavia Zuber, Katharina Maniura-Weber, and Qun Ren, Role of the Surface Nanoscale Roughness of Stainless Steel on Bacterial Adhesion and Microcolony Formation, ACS Omega 2018, 3, 6456−6464; http://dx.doi.org/10.1021/acsomega.8b00769.

[10] E. A. Specht, E. Braselmann, and A. E. Palmer, A critical and comparative review of fluorescent tools for live-cell imaging, Annu. Rev. Physiol., vol. 79, pp. 93–117, 2017; https://doi.org/10.1146/annurev-physiol-022516-034055 .

[11] D. G. Allison and M. A. Sattenstall, The influence of green fluorescent protein incorporation on bacterial physiology: a note of caution, J. Appl. Microbiol., vol. 103, pp. 318–324, 2007.

[12] Trainer, K., Nazarova, D., Naydenova, I., Toal, V., 2010. Optimization of an acrylamide-based photopolymer system for holographic inscription of surface patterns with sub-micron resolution. J. Opt. 12, 124012.

[13] Boiko, Y.B., Solovjev, V.S., Calixto, S., Lougnot, D.-J., 1994. Dry photopolymer films for computer-generated infrared radiation focusing elements. Appl. Opt. 33, 787. https://doi.org/10.1364/AO.33.000787

[14] Pavani, K., Naydenova, I., Martin, S., Toal, V., 2007. Photoinduced surface relief studies in an acrylamide-based photopolymer. J. Opt. A: Pure Appl. Opt. 9, 43–48. https://doi.org/10.1088/1464-4258/9/1/008

[15] Croutxé-Barghorn, C., Lougnot, D.J., 1996. Use of self-processing dry photopolymers for the generation of relief optical elements: a photochemical study. Pure Appl. Opt. 5, 811–825. https://doi.org/10.1088/0963-9659/5/6/007

[16] Smirnova, T.N., Sakhno, O.V., 2002. A mechanism of the relief-phase structure formation in self-developing photopolymers. Opt. Spectrosc. 93, 126–131. https://doi.org/10.1134/1.1496735

[17] Yoda, I., Koseki, H., Tomita, M., Shida, T., Horiuchi, H., Sakoda, H., et al. (2014). Effect of surface roughness of biomaterials on Staphylococcus epidermidis adhesion. BMC Microbiol. 14:234. doi: 10.1186/s12866-014-0234-2

[18] Ange Lu, Yan Gao, Tan Jin, Xichun Luo, Quanren Zeng, Zhentao Shang,Effects of surface roughness and texture on the bacterial adhesion on the bearing surface of bio-ceramic joint implants: An in vitro study,Ceramics International,Volume 46, Issue 5,2020,Pages 6550-6559,ISSN 0272-8842,

[19] Xing, R., Lyngstadaas, S. P., Ellingsen, J. E., Taxt-Lamolle, S., and Haugen, H. J. (2015). The influence of surface nanoroughness, texture and chemistry of TiZr implant abutment on oral biofilm accumulation. Clin. Oral. Implants Res. 26, 649–656. doi: 10.1111/clr.12354

[20] T. Wassmann, S. Kreis, M. Behr, R. Buergers, The influence of surface texture and wettability on initial bacterial adhesion on titanium and zirconium oxide dental implants, Int. J. Implant Dent. 3 (2017) 32.

[21] S. Eick; E. Glockmann; B. Brandl; W. Pfister (2004). Adherence of Streptococcus mutans to various restorative materials in a continuous flow system. , 31(3), 278–285.

[22] D. Dutra, G. Pereira, K. Kantorski, R. Exterkate, C. Kleverlaan, L. Valandro, F. Zanatta, Grinding with diamond burs and hydrothermal aging of a Y-TZP material: effect on the material surface characteristics and bacterial adhesion, Oper. Dent. 42 (2017) 669–678

[23] Escuti, MJ and Crawford, PJ 2004, '*Holographic photonic crystals'*, 'Society of photo-optical engineers', 43.

[24] Rory Staines, March 2020, '*Inscription of periodical Surface structures in photopolymer material by multiple beam holographic recording',* BSc thesis.